Featured in Physics

Low-Level Cloud Radiative Forcing Enhances Wind-Farm Wake Recovery

Davide Selvatici [*] and Richard J. A. M. Stevens [†]

Physics of Fluids Group, Max Planck Center Twente for Complex Fluid Dynamics, J. M. Burgers Center for Fluid Dynamics, University of Twente, P.O. Box 217, Enschede, 7500 AE, The Netherlands

(Received 23 December 2025; revised 9 May 2026; accepted 24 June 2026; published 2 September 2026)

Recent simulations and observations suggest that clouds interact with offshore wind farms, yet the physical mechanisms governing this interaction remain unclear. Here, we investigate these processes using large-eddy simulations of stratocumulus-topped boundary layers, systematically removing key forcings to isolate their physical effects. We consider three progressively simplified scenarios: (i) a fully developed marine stratocumulus boundary layer, (ii) a case without radiative forcing, which weakens both cloud-top longwave cooling and entrainment, and (iii) a clear-sky case in which both radiative forcing and liquid water are removed. The presence of cloud-top radiative cooling increases entrainment, leading to a less stable and deeper boundary layer that promotes vertical transport of momentum and energy toward the turbines. This leads to a faster wake recovery, with direct implications for the performance of neighboring wind farms. Overall, our results demonstrate that radiatively driven cloud-top entrainment is a key mechanism linking cloud dynamics to the performance of large wind farms and underscore the need for wind-energy models that explicitly represent interactions among wind farms, the atmosphere, and cloud processes.

DOI: 10.1103/86lm-1nr3

I. INTRODUCTION

Observations show that stable atmospheric conditions favor the formation of long wind-farm wakes, which can extend up to 70 km downstream [1]. Such conditions are common offshore, where wakes from neighboring wind farms can adversely affect power production [2]. As offshore wind development accelerates, cumulative interactions between wind farms and the atmosphere intensify and therefore warrant further investigation [3]. Kirby *et al.* [4] identify two primary mechanisms through which wind farms interact with the atmosphere. The first involves turbine-scale losses caused by wakes from upstream turbines. The second arises from the combined influence of the entire wind-farm array and leads to farm-scale losses by reducing the average wind speed across the wind farm. For large wind farms, these farm-scale losses are typically more than twice as large as turbine-scale losses [5]. In such cases, wind farms impact the large-scale structure of the atmospheric boundary layer, making the farm-wake recovery process slower.

Atmospheric stratification plays a central role in these processes by regulating momentum entrainment into wind farms [8,9]. Lanzilao and Meyers [10] showed that both inversion-layer strength and tropospheric stratification strongly affect power output and identified the wind-farm collective behavior by comparing the wind farm with a single turbine under identical conditions. More recently, Lanzilao and Meyers [11] isolated the effect of inversion-layer height, demonstrating that deeper boundary layers promote faster wake recovery through enhanced vertical momentum entrainment. Stieren *et al.* [12] and Kasper *et al.* [13] further demonstrated that horizontal temperature gradients, for example, due to land-sea transitions, can substantially modify wind farm-atmosphere interactions. Such modifications arise from warm or cold advection and the associated geostrophic shear and differ from those in barotropic conditions.

Among the atmospheric phenomena characteristic of offshore environments, marine clouds remain mostly unstudied, despite their prevalence in large offshore wind-farm regions. Figure 1 compares the global distribution of operating wind farms as of 2024 with the mean annual cloud coverage for all cloud types, compiled from 1971 to 1996 over land and 1954 to 1997 over ocean [6,7,14]. Regions with a high density of wind farms also exhibit substantial cloud coverage, indicating that interactions

[*]Contact author: d.selvatici@utwente.nl
[†]Contact author: r.j.a.m.stevens@utwente.nl

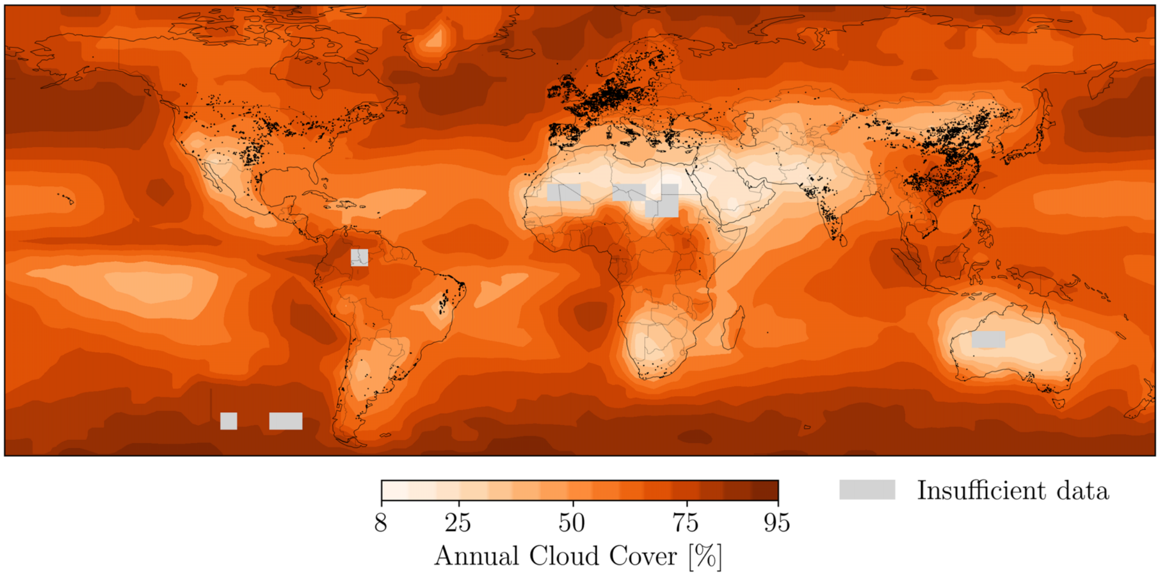

FIG. 1. Geographical distribution of annual cloud cover and locations of operating wind farms. Black dots indicate turbine positions based on the GWEC database [6]. The color map shows mean cloud cover derived from data collected between 1971 and 1996 over land and between 1954 and 1997 over the ocean (Hahn and Warren [7]).

between clouds and wind-farm cluster performance warrant further investigation. When considering only low-level clouds, such as stratus and stratocumulus, annual cloud coverage exceeds 30% in the North Sea and 35% along the eastern Chinese coast. These regions host some of the densest offshore wind-farm clusters worldwide [6,14].

Low-level clouds, particularly stratocumulus, are sustained by a radiatively driven convective instability at the cloud top [14,15]. The associated strong net radiative cooling, typically 50–90 W/m^2, generates turbulent fluctuations that entrain warm and dry air from the free troposphere into the boundary layer [16]. The resulting cooling rates at the top of the atmospheric boundary layer, $\sim$5–10 K/h, are much larger than typical surface heating or cooling rates, which are usually below ± 1 K/h [15–17]. Compared with clear-sky conditions, cloud-top cooling strongly enhances turbulent entrainment and accelerates the growth of the inversion-layer height [14,18]. The presence of clouds also leads to a marked increase in turbulent kinetic energy within the boundary layer [19,20]; therefore, the presence of such cloud processes is expected to influence wind-farm-scale losses and wake recovery. Finally, it is worth mentioning that the presence of wind farms, in turn, can significantly affect the development of the cloud itself. Recent simulations and measurements have shown that wind-farm-induced blockage and wakes can perturb the cloud layer. They can increase liquid water near the farm entrance and decrease it farther downstream, with measurable effects on cloud radiative properties and precipitation, indicating that wind-farm-cloud interaction is bidirectional [21–24].

Understanding these complex processes requires capturing both cloud-top turbulence and wind-farm flow accurately. Large-eddy simulations (LES) provide such a framework and accurately represent cloud dynamics when the grid spacing is sufficiently fine to capture small-scale convection [25–27]. In this work, we present a systematic LES study of how low-level clouds influence wake recovery in offshore wind farms, using high-resolution simulations of stratocumulus-topped boundary layers (STBLs) across a range of atmospheric conditions. We first perform an ensemble analysis to isolate the role of cloud-top radiative cooling and then simulate an offshore wind farm under three representative conditions: a fully developed STBL, a case without radiative cooling, and a clear-sky case without liquid water. The analysis focuses on turbulent energy entrainment, wake-induced turbulent kinetic energy, and the mechanisms governing wind farm-atmosphere interactions in the presence of clouds.

The rest of the paper is organized as follows. Section II describes the numerical methodology and Sec. III introduces the parameter space used to isolate the effects of cloud-radiative forcing. Section IV presents the atmospheric inflow conditions considered for the wind-farm simulations, while Sec. V explains their numerical setup. The impact of the wind farm on turbulent kinetic energy is analyzed in Sec. VI, followed by an examination of wake recovery in Sec. VII. Section VIII assesses wind-farm power performance and Sec. IX investigates the wake energy budget. Finally, Sec. X summarizes the main findings and offers concluding remarks.

II. NUMERICAL METHOD

The simulations use an in-house LES framework that has been applied extensively to wind-energy and atmospheric-flow problems (e.g., [12,13,28–30]). The code has been extended to simulate clouds and has been validated for both precipitating and nonprecipitating STBLs using observations from the second dynamics and chemistry of marine stratocumulus field study (DYCOMS-II RF01) and atlantic stratocumulus transition experiment (ASTEX) field campaigns [25,27].

The code employs a pseudospectral scheme with spectral derivatives in the horizontal directions and second-order centered finite differences in the vertical. The 3/2 dealiasing rule removes aliasing errors from the nonlinear terms, yielding a nondissipative discretization [31]. Double-periodic boundary conditions are applied horizontally [32–34]. Time integration uses a third-order Adams-Bashforth scheme with a constant Courant-Friedrichs-Lewy number of 0.1. Surface fluxes follow Monin-Obukhov similarity theory [32]. Subgrid-scale stresses and scalar fluxes are modeled with the anisotropic minimum dissipation (AMD) formulation [29,35,36].

The LES solves the anelastic form of the Navier-Stokes equations, which retain weak compressibility effects while filtering acoustic waves. Unlike the Boussinesq approximation, the anelastic formulation accounts for vertical density stratification and is therefore well suited for simulations of STBLs [25,37,38]. The reference density profile $\rho_{\text{ref}} = \rho_{\text{ref}}(z)$ is time invariant and obtained from the initial moisture scalars through hydrostatic balance. With this choice, the governing equations can be written as

$$\nabla \cdot (\rho_{\text{ref}} \tilde{u}) = 0, \tag{1}$$

$$\frac{\partial \tilde{u}}{\partial t} + (\tilde{u} \cdot \nabla)\tilde{u} = -1/\rho_{\text{ref}} \nabla \tilde{p}^* + \nabla \cdot \tilde{\tau} + f_c(\tilde{u} - U_G) + g\beta + F_T, \tag{2}$$

$$\frac{\partial \tilde{h}}{\partial t} + (\tilde{u} \cdot \nabla)\tilde{h} = 1/\rho_{\text{ref}} \nabla \cdot (\rho_{\text{ref}} k_h \nabla \tilde{h}) - \nabla \cdot R + \omega \partial_z \tilde{h}, \tag{3}$$

$$\frac{\partial \tilde{q}_t}{\partial t} + (\tilde{u} \cdot \nabla)\tilde{q}_t = 1/\rho_{\text{ref}} \nabla \cdot (\rho_{\text{ref}} k_{q_t} \nabla \tilde{q}_t) + \omega \partial_z \tilde{q}_t. \tag{4}$$

where the symbol $\tilde{\cdot}$ denotes the LES filtering operator. Equations (1) and (2) represent the continuity and momentum equations. Here u is the resolved velocity field; $\tilde{p}^*$ is the modified pressure that enforces the continuity constraint; $\tilde{\tau}$ is the SGS stress tensor and $\tau_{ij} = \widetilde{u_i u_j} - \tilde{u}_i \tilde{u}_j$ is its deviatoric and traceless part, while the trace of the SGS stress tensor $\tau_{kk}^t/3$ is absorbed into the modified pressure $\tilde{p}^*$; f_c is the Coriolis frequency; U_G is the geostrophic velocity in the free troposphere; $g = 9.81\ \text{m/s}^2$ is the gravitational acceleration; and F_T is the turbine-induced forcing (see Sec. V). The momentum and continuity equations are coupled to the moisture equations through the buoyancy parameter $\beta = (\rho_{\text{ref}} - \rho)/\rho_{\text{ref}}$.

Equations (3)–(6) govern the evolution of the moisture fields, where q_t is the total water content (the sum of vapor and liquid water specific humidities, $q_t = q_v + q_l$), and h is the liquid-water static energy, defined as the sum of enthalpy and potential energy,

$$h = [c_d + q_t(c_v - c_d)]T - q_l L_v + gz, \tag{5}$$

where c_d, c_v, and c_l are the specific heat capacities of dry air, water vapor, and liquid water, respectively; $L_v = L_v(T)$ is the temperature-dependent latent heat of vaporization [26,37]; and z is the vertical coordinate. The coefficients k_h and k_{q_t} are the diffusivities, modeled with the same AMD formulation used for the subgrid-scale stresses. The large-scale subsidence velocity is prescribed as $\omega = \omega_0 z$, where ω_0 is the imposed subsidence rate.

From h and q_t, the liquid-water specific humidity q_l is obtained iteratively from

$$q_l = q_t - q_v + \delta \frac{\partial q_l}{\partial q_t}\left(\log(2) - \log\left(\tanh\left(\frac{q_t - q_{\text{sat}}}{2\delta}\right) + 1\right)\right), \tag{6}$$

where q_v is obtained iteratively using an eighth-order polynomial approximation to the Clausius-Clapeyron relation [37,39].

Finally, the term R represents the longwave radiative forcing. Following Chung *et al.* [40], the net longwave radiative forcing is modeled as

$$R = F_0 e^{-\kappa \text{LWP}(z)} + Cz, \tag{7}$$

where LWP is the liquid water path, which represents the vertically integrated liquid water content and is defined as

$$\text{LWP}(x, y, z, t) = \int_z^{L_z} \rho_{\text{ref}}(z) q_l(x, y, z', t) dz', \tag{8}$$

where L_z is the vertical extent of the computational domain. In Eq. (7), C is a constant representing the longwave radiative cooling in the free troposphere, set to $C = 0.024\ \text{W/m}^3$ following Chung *et al.* [40], which can be used also in cases without liquid water (where $\text{LWP} = 0$) or without radiative cooling, as further explained in the next sections. A tropospheric relaxation term is applied following Bretherton *et al.* [41] to counteract subsidence warming above the boundary-layer top. Because of the additional state variables and the vertical integration required for the radiative forcing, these equations carry a substantially higher computational cost than conventional LES under cloud-free conditions.

As reference values for the thermodynamic constants and initial profiles, we adopt measurement-based parameters from the ASTEX campaign, which are representative of typical STBLs [17,27,40,41]. The initial inversion height is $H_0 = 662.5$ m. The Coriolis parameter is $f_c = 8.7 \times 10^{-5}$ s^{-1}, representative of the latitude at which ASTEX measurements were taken [42]. The surface roughness length is $z_0 = 2 \times 10^{-4}$ m, characteristic of open-sea conditions [27]. Parameters not specified here are defined in the corresponding sections.

III. ENSEMBLE ANALYSIS

To investigate the effect of radiative forcing on atmospheric convection in a typical marine STBL, we systematically vary the subsidence rate, sea-surface temperature, relative geostrophic velocity, inversion-layer strength, total water-humidity difference, and net shortwave radiative forcing. The initial conditions for all cases are summarized in Table I and compared with values from the ASTEX LES database by van der Dussen *et al.* [27] and the study by Chung *et al.* [40]. These studies include cases with low cloud cover and stratocumulus-to-cumulus transitions and therefore cover a broader parameter space than the present study. Here, we focus on well-sustained cloud decks. The simulations share the same initialization and are grouped into two sets: (i) 64 cases representing a typical marine STBL and (ii) 64 cases in which cloud-top longwave radiative cooling is suppressed [$F_0 = 0$ in Eq. (7)]. This yields a total of 128 simulations.

A uniform horizontal grid spacing of 62.5×62.5 m^2 is used. The vertical spacing is 10 m up to an altitude of 2 km, above which the grid is gradually stretched to a maximum spacing of 40.7 m at the top of the domain. The computational domain has dimensions of $2 \times 2 \times 3.5$ km^3. Test simulations conducted with higher resolution or larger domain size showed no significant differences in the reported steady-state results, supporting the use of the chosen setup [27,40]. Following Chung *et al.* [40], the boundary conditions are prescribed as constant in time to allow the system to reach statistically steady conditions, consistent with the approach of van der Dussen *et al.* [43]. Each simulation is integrated for 110 h to ensure statistical stationarity.

The goal is to isolate the effect of radiative forcing on atmospheric convection in a typical marine STBL. To this end, a second group of simulations removes the main source of cloud-top cooling, allowing us to examine how surface fluxes, entrainment, and subsidence maintain turbulence when the cloud layer is no longer driven by radiation. In simulations that include radiative cooling, the cloud-top radiative flux F_0 in Eq. (7) is estimated using the rapid radiative transfer model (RRTMG) full-radiative scheme [44]. For cases with $\Delta q_t = -1.1$ g kg^{-1}, $F_0 = 74$ W m^{-2}, consistent with Chung *et al.* [40], while for $\Delta q_t = -4.6$ g kg^{-1}, $F_0 = 90$ W m^{-2}. Both day- and nighttime conditions are considered, with solar shortwave heating parametrized using the delta-Eddington approximation with a solar constant of 1376 W/m^2 and a zenith angle of 52°, following van der Dussen *et al.* [43]. The daytime shortwave heating partially offsets cloud-top radiative cooling and reduces the inversion-layer height in both cases, thereby decreasing the liquid-water content. We define the inversion height as the level where q_l rapidly decreases to zero, or equivalently, the height of the maximum gradient of h and q_t. Although several definitions of z_i are possible, the strong capping inversion ensures that differences among them are within a few tens of meters. The parameter space explored corresponds to typical offshore conditions, where surface heating is relatively weak, as in persistent marine stratocumulus decks.

Figure 2 compares the steady-state cloud-top heights from all simulations. Panel (c) shows the ensemble-mean inversion height across the full parameter space. In all cases, the STBL is deeper than in the corresponding simulations without radiative cooling. This difference results from longwave cooling by liquid water, which enhances convective instability and promotes entrainment of free-tropospheric air [14,16]. The associated increase in entrainment raises the boundary-layer top. For the STBL cases, $\bar{z}_i \approx 1.25$ km, whereas for the cases without radiative cooling $\bar{z}_i \approx 0.39$ km. The larger boundary-layer depth in the STBL cases implies a greater available momentum flux, which is expected to affect wind-farm wake recovery.

Supporting the ensemble analysis, Stevens [18] showed that boundary-layer growth under cloudy conditions is faster than in cloud-free cases, consistent with our results.

TABLE I. Description of the atmospheric and sea-surface conditions considered, resulting in a total of 128 simulations. The left column lists the perturbed variables, and the middle and right columns report the numerical values used and, for comparison, the minimum and maximum values corresponding to the STBL simulations by van der Dussen *et al.* [27] and Chung *et al.* [40] using LES.

Variable	Present work	ASTEX LES [27]	Chung *et al.* [40]
Subsidence rate ω_0	$(4, 9) \times 10^{-6}$ s^{-1}	$(1, 5) \times 10^{-6}$ s^{-1}	$(8, 9) \times 10^{-6}$ s^{-1}
Sea-surface temperature SST	(290.3, 292.5) K	(290.3, 294.6) K	(293, 300) K
Geostrophic velocity u_G	(6, 10.2) m/s	(3.1, 10.2) m/s	10.44 m/s
Inversion strength $\Delta\theta_l$	(5.5, 10.5) K	(4, 5.7) K	5 K
Total humidity difference Δq_t	(−4.6, −1.1) g/kg	(−3, −1) g/kg	−0.9 g/kg
Net shortwave radiative flux	(Day, night)	(Day, night)	Night
Radiative cooling	(Active, not active)	Active	Active

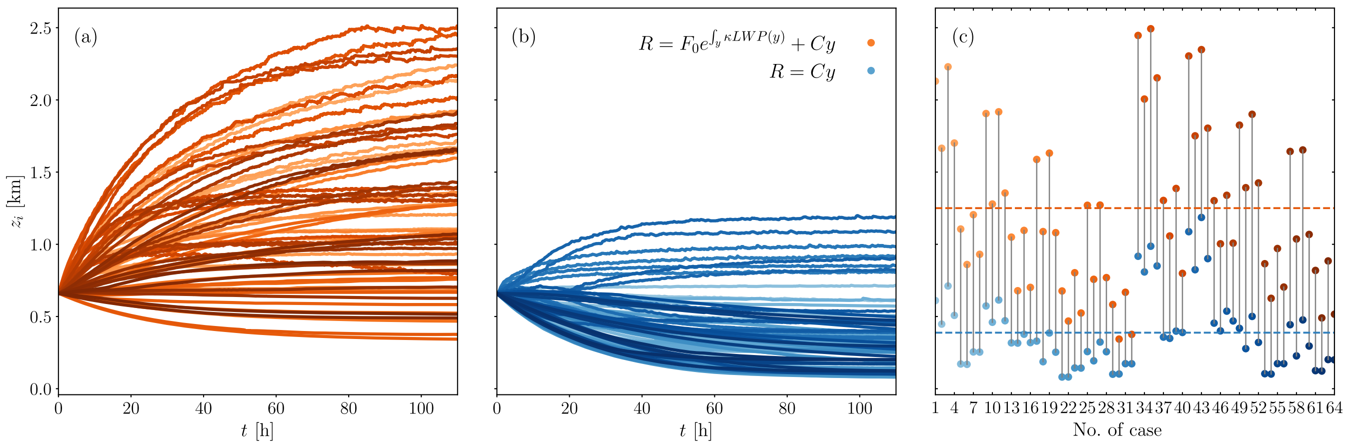

FIG. 2. Evolution of the inversion-layer height across the sensitivity ensemble (see also Table I). (a) Cloud-top evolution in simulations that include radiative cooling. (b) Same as (a), but with $F_0 = 0$ [Eq. (7)]. (c) Comparison between the two sets of simulations. The orange dashed line in panel (c) indicates the ensemble-mean cloud top from simulations in (a), and the blue dashed line shows the one representative case from (b).

Likewise, Mehta *et al.* [45] reported that low-level clouds confined within the atmospheric boundary layer, such as stratus and stratocumulus, promote deepening through enhanced cloud-top entrainment. Observations by Koning *et al.* [46] at the Cabauw observatory in The Netherlands further indicate that the mixed-layer top is higher when clouds are present than under clear-sky conditions, while surface-layer temperature fluxes remain essentially unchanged. Finally, the cooling induced by the cloud-top radiative jump typically reaches 5–10 $\mathrm{K\,h^{-1}}$ [14], which exceeds typical surface-heating rates that are generally below 1 $\mathrm{K\,h^{-1}}$ [17]. As a result, cloud-top cooling drives stronger boundary-layer growth through entrainment than surface heating and convection.

In the present simulations, identical initial and boundary conditions are used within each pair of cases to isolate the effect of radiative cooling, which would otherwise be coupled with additional processes. Under strong daytime solar radiation, however, reduced cloud albedo in the radiative-free cases could lead to higher surface temperatures. Determining the conditions under which boundary-layer growth driven by surface warming exceeds that induced by radiative cooling is left for future investigation. The parameter space examined here is representative of typical offshore North Sea environments at operating wind farms where surface warming by shortwave radiation is relatively weak. Finally, we focused on fully developed cloud decks with strong radiative properties. Thin clouds with low cloud cover could have less influence on the boundary-layer structure and thus on the wind-farm wake recovery.

IV. ATMOSPHERIC INFLOW CONDITIONS

Two nocturnal cases representative of the explored parameter space are used for the wind-farm simulations. A third scenario sets $q_l = 0$, removing all cloud liquid water and providing a clear-sky baseline without radiative or cloud-driven processes. The cases are intentionally idealized and are not meant to reproduce the real atmosphere. Instead, they form a simple hierarchy in which individual forcings are progressively removed. This approach enables us to identify how cloud-top radiative cooling and cloud liquid water each influence boundary-layer evolution and structure.

The STBL case, referred to as case A, uses the radiative formulation in Eq. (7) with $F_0 = 74\ \mathrm{W/m^2}$ and $\kappa = 130\ \mathrm{m^2/kg}$, following Chung *et al.* [40] and using the RRTMG scheme. The second configuration, case B, is radiative-free and uses $F_0 = 0\ \mathrm{W/m^2}$. The third configuration, case C, is cloud-free, and it is obtained by setting $q_l = 0$, so $\mathrm{LWP} = 0$, removing radiative cooling by consequence. Cloud-free boundary layers are driven only by surface heating. In contrast, net radiative cooling at the top of the boundary layer occurs only when liquid water is present [14,16]. As a result, the only difference between cases B and C is the buoyancy contribution from liquid water.

The three cases are initialized with identical vertical profiles and share the same boundary conditions. Below the initial inversion height, h and q_t are set to 295 kJ/kg and 10.2 g/kg, respectively. The inversion strength is $\Delta h = 5$ kJ/kg (equivalent to $\Delta\theta_l = 5.5$ K), and $\Delta q_t = -1.1$ g/kg. Above z_i, the lapse rate of h is 5.2 kJ/(kg km), and the lapse rate of q_t is -2.8 g/(kg km). To avoid negative values, q_t is relaxed exponentially to zero above $z = 3$ km [27,47]. The geostrophic wind speed is $U_G = 10.2$ m/s. The large-scale subsidence rate is $9 \times 10^{-6}\ \mathrm{s^{-1}}$, the sea-surface temperature is 291 K, and the surface pressure is 1.029 bar [40]. In these cases, shortwave radiative heating is disabled to represent nocturnal conditions.

TABLE II. Overview of the marine atmospheric boundary-layer cases considered in this study. Case A corresponds to a STBL. Case B imposes zero net radiative forcing [Eq. (7)]. Case C sets the liquid-water specific humidity to zero ($q_l = 0$).

Case	Description	z_i [km]
A	STBL	1.20
B	$F_0 = 0$ W/m^2	0.39
C	$q_l = 0$ g/kg	0.28

These cases are run at higher resolution in a domain of $5 \times 5 \times 3$ km^3, discretized with $180 \times 180 \times 384$ grid points in the streamwise, spanwise, and vertical directions. This corresponds to a horizontal grid spacing of 27.78×27.78 m^2. The vertical spacing is 5 m up to an altitude of 1.5 km, above which it gradually increases. This configuration provides the resolution needed for the subsequent wind-farm simulations. Each case is integrated for 100 h to reach a statistically steady state, after which the domain is extended to include the wind farm. This strategy reduces computational cost and has been used in previous studies [11,48,49]. The Appendix presents the convergence of z_i, LWP, and u_*.

Table II summarizes the boundary-layer height for the three cases, and Fig. 3 shows the corresponding steady-state vertical profiles. Here, the liquid-water potential temperature is defined as $\theta_l = \theta \exp[-q_l L_v/(c_p T)]$, where θ is the dry-air potential temperature [50]. The inversion-layer height, defined as the level where θ_l and q_t have their maximum gradients, varies across the cases. Cloud-top radiative cooling creates convective instability that strengthens the entrainment of free-tropospheric air [14,16], thereby opposing the downward motion caused by subsidence. When radiative cooling is reduced (cases B and C), this convective enhancement weakens, and the inversion height decreases. In those cases, the boundary layer is lower, as it is driven only by surface sensible and latent heat fluxes. It is worth mentioning that the moist boundary-layer conditions considered for the wind-farm cases are realistic atmospheric conditions, but they are not intended to span the full range of possible conditions. A broader exploration of the effect of inversion strength, cloud properties, moisture content, and atmospheric stability would be valuable but is beyond the scope of the present study.

The inversion-layer heights in cases A and B, being $z_i = 1.2$ km and $z_i = 0.39$ km, respectively, closely match the values of the ensemble average. The lower inversion height in case C ($z_i = 0.28$ km) is a consequence of the absence of liquid water, which decreases buoyancy by modifying the temperature stratification in the cloud layer and reducing the counteracting force to subsidence when compared to case B. In case A, cloud-top convective instability produces a localized peak in k near the cloud top and raises k throughout the boundary layer [Fig. 3(d)]. This region overlaps with a peak in q_l, creating a local maximum in LWP that strengthens radiative forcing and further enhances turbulence. As a result, this cloud-top peak is absent in cases B and C, which show only the near-surface maximum in k associated with velocity shear.

Correspondingly, the turbulence intensity at hub height, defined as $\mathrm{TI} = \sqrt{u'^2 + v'^2}/\sqrt{u^2 + v^2}$, is higher in case A (10%) than in cases B (5.6%) and C (5.2%). Consistent with these trends across the parameter space analyzed in Sec. III, the STBL simulations feature a higher TI at hub height in all cases except three in which the gap between the two pairs of simulations is close to zero. In general, we observe that the lower the cloud-layer height, the stronger its influence on the turbulent kinetic energy. For higher-altitude and decoupled clouds, the vertical mixing in the lower part of the boundary layer is reduced, decreasing the differences in TI at hub height but producing a higher

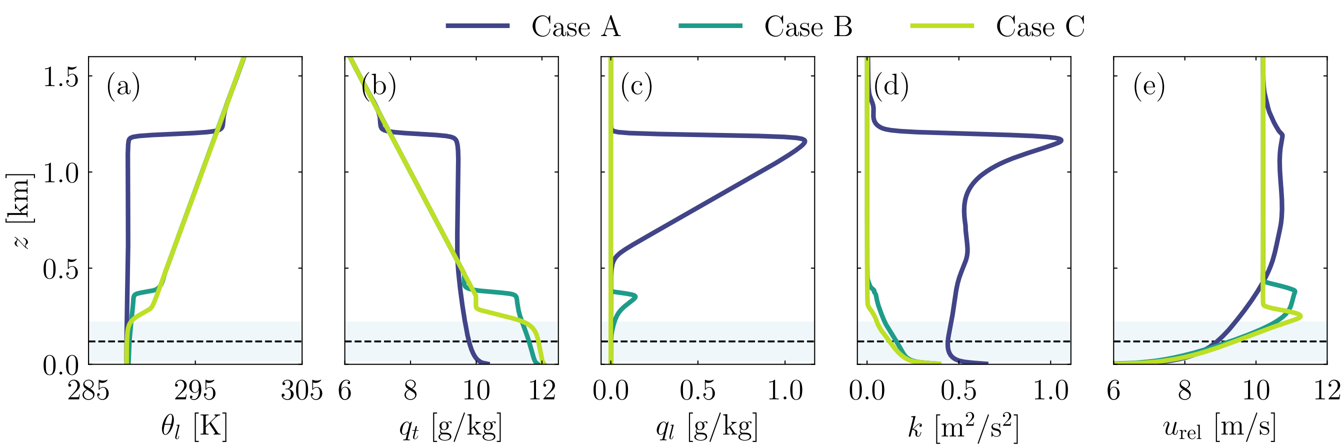

FIG. 3. Characterization of the marine atmospheric boundary layer for cases A, B, and C (see Table II), showing (a) liquid-water potential temperature, (b) total-water specific humidity, (c) liquid-water specific humidity, (d) turbulent kinetic energy (k), and (e) relative velocity magnitude. Statistics are averaged over the final 2.5 h of each simulation. The light-blue region marks the area swept by the turbine rotors, and the dashed line indicates the hub height.

turbulent kinetic energy in the higher regions of the boundary layer.

Differences in boundary-layer structure have a pronounced effect on the velocity profiles [Fig. 3(e)]. Because the boundary layer is deeper in case A, the shear within the rotor region is lower than in the other cases. In contrast, cases B and C show velocity peaks near the rotor-top height, corresponding to super-geostrophic jets typical of nocturnal boundary layers [51–54]. The resulting hub-height velocity is lower in case A ($u_{\mathrm{hub}} = 8.9$ m/s) than in the other two cases ($u_{\mathrm{hub}} = 9.2$ m/s for case B and $u_{\mathrm{hub}} = 9.4$ m/s for case C). The horizontal momentum within the boundary layer, i.e., $\int_0^{z_i} u_{\mathrm{rel}}(z)dz$ in case A, is approximately 3.1 times larger than in case B and 4.5 times larger than in case C, mainly due to the higher boundary-layer height [see Fig. 3(e)]. This trend is observed in all cases of the parameter space considered in Sec. III. As described in the following, the higher momentum availability is among the factors contributing to the wind-farm wake development and energy transfer in the boundary layer.

V. WIND-FARM CHARACTERIZATION AND SIMULATION

To represent a characteristic mid-sized offshore wind farm, we consider a 9×5 staggered wind-farm array with a spacing of $5D$ in both the streamwise and spanwise directions, using the IEA 10 MW offshore reference turbine [55,10]. This turbine has a rotor diameter of $D = 198$ m, a hub height of 119 m, and a thrust coefficient of $C_T = 0.88$ [55]. The location of the wind farm within the computational domain is shown in Fig. 4. A proportional-integral controller maintains the planar-averaged wind direction at hub height at 0° [56]. Turbines are represented using the Actuator Disk Model with a correction for low-resolution effects [57], which is well suited for capturing large-scale interactions between wind farms and atmospheric dynamics when large-scale atmospheric effects are studied, as shown by Wu and Porté-Agel [58,59] and Stevens *et al.* [60].

The steady-state conditions described above provide the inflow for the wind-farm simulations. The inflow is generated using the concurrent precursor method [61], combined with the improved fringe-region technique of Lanzilao and Meyers [49], which ensures that the flow entering the wind-farm domain remains undisturbed. In this approach, a secondary domain without turbines is simulated alongside the wind-farm domain, and at each time step, a portion of its flow field is copied into the fringe region (Fig. 4). To simulate large-scale wind farm-atmosphere interactions, we use a computational domain of $70 \times 15 \times 10$ km^3, discretized with $2520 \times 540 \times 650$ grid points in both the concurrent and precursor domains. The horizontal grid spacing is 27.78 m, while the vertical spacing is 5 m up to an altitude of 1.5 km. Above this height, the grid is gradually stretched, reaching a maximum vertical spacing of 45.5 m at the domain top. This discretization provides a consistent and computationally efficient framework for resolving both wind-energy and cloud-physics processes (see, e.g., [10,12,13,27,40]).

To extend the initialization simulation to the target domain size, we employ the tiling technique [11,48,49], while preserving the same grid resolution. In the free troposphere, where turbulent fluctuations are weak, the flow is vertically extrapolated [49]. After the expansion of the domain, the flow evolves for one physical hour before the wind farm is introduced. The simulation then continues for an additional 3.5 h, after which statistics are collected over a two-hour averaging period. In total, 6.5 h of flow evolution are simulated in the extended domain, following 100 h of spin-up in the initialization domain.

VI. WIND FARM EFFECT ON TURBULENT KINETIC ENERGY

Wind turbines perturb the incoming flow through their forcings, which promote mixing and enhance turbulent

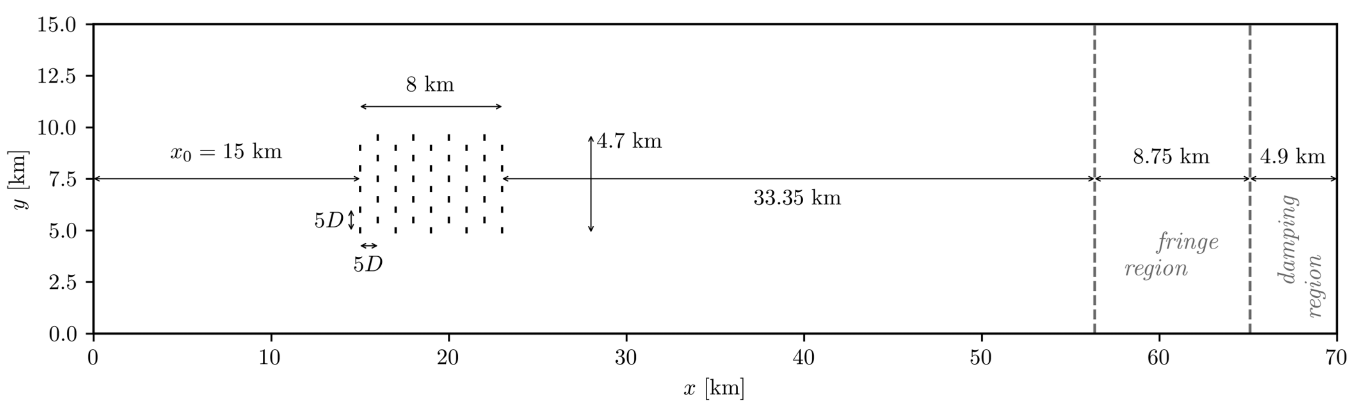

FIG. 4. Characterization of the numerical domain used for the wind-farm simulations. The vertical domain height is 10 km. The right side of the domain contains a fringe region that applies the forcing prescribed by the concurrent precursor method [61]. The damping region corresponds to the advection damping introduced through the fringe-region technique [49,62].

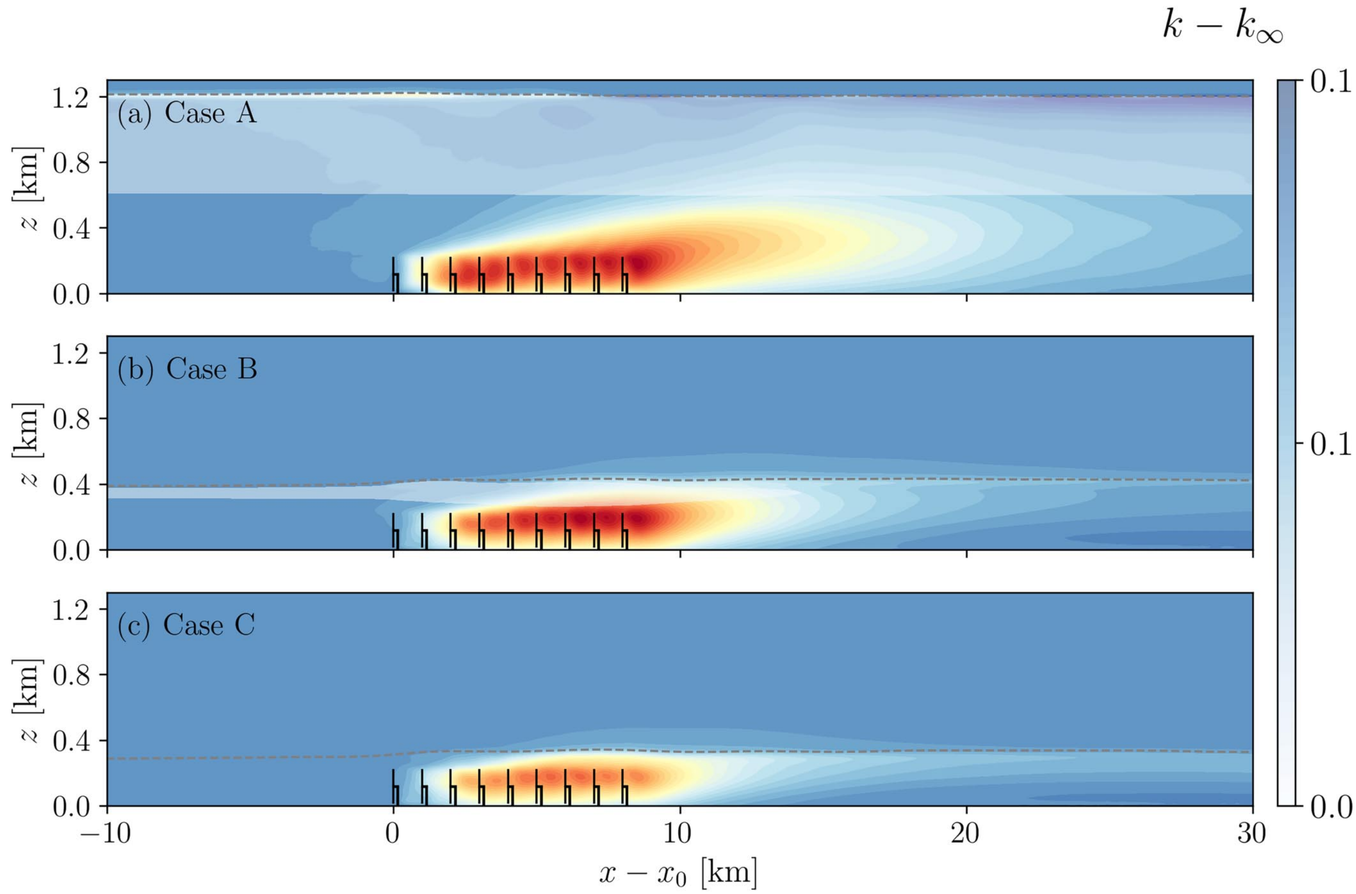

FIG. 5. Comparison of the wind farm-induced changes in horizontally averaged turbulent kinetic energy (k) for cases A, B, and C, relative to the inflow value. Gray dashed line indicates the inversion-layer height, and the superimposed white regions delineate regions which contain liquid water, i.e., where $\langle q_l \rangle > 0$.

motion in their wakes. Figure 5 shows the wind farm-added turbulent kinetic energy, k, for the three considered cases, defined as $k = 1/2(\langle u'^2 \rangle + \langle v'^2 \rangle + \langle w'^2 \rangle)$, where u', v', and w' denote the velocity fluctuations in the streamwise, spanwise, vertical directions, respectively, and $\langle \square \rangle$ denotes time averaging. The extent of the regions with enhanced mixing depend on the inflow velocity profile, atmospheric stability, and turbulent entrainment into the wind farm from above and the sides, which together control the rate of flow recovery to the inflow conditions [8,9,63].

In case A, the wake-added k is visible up to approximately $z \sim 0.8$ km and extends more than 35 km downstream. Its downstream development is different in the other cases, in which the peak of wake-added k develops for shorter distances. Moreover, it is confined vertically to roughly $z \sim 0.4$ km in cases B and C. This difference primarily results from variations in the inversion-layer height and strength, which are influenced by cloud-top radiative cooling. In shallow boundary layers (cases B and C), the wake cannot penetrate above the capping inversion at the top of the atmospheric boundary layer. As a result, only a limited amount of turbulence penetrates above the inversion, as reflected by the weak increase in k at those heights. In the STBL case (case A), this constraint is absent, allowing access to a larger momentum reservoir within the boundary layer, which can be beneficial for wind-farm wake recovery.

The wind farm also affects the inversion-layer height, indicated by the gray dashed lines (Fig. 5). In all three cases, the boundary-layer height starts to fluctuate near the wind-farm entrance, as a consequence of the wind-farm-induced gravity waves, a pressure perturbation that can extend for tens of kilometers around the wind farm [10,64–66]. Moreover, in the cases that feature the presence of liquid water (A, B), the wind farm influence extends up to that height, causing visible effects on the cloud evolution. For example, in case A, the cloud top is deformed, and in case B, the liquid water humidity slightly enlarges over the wind farm and reduces downstream, evaporating completely. Although the absence of radiative cooling in case B could facilitate this abrupt effect on a cloud, preliminary simulations performed using different atmospheric conditions and similar boundary-layer heights have shown that this effect can happen also in a full STBL. In general, these changes have a significant impact on cloud-layer dynamics, with direct consequences for cloud liquid-water content and its radiative properties [21].

VII. WIND-FARM WAKE RECOVERY

Figure 6 compares the average hub-height velocity across the three cases and reveals clear differences in wake recovery related to the boundary-layer structure, as shown by the 90% velocity threshold relative to the inflow. Figure 6(d) reports the streamwise velocity averaged in the wind-farm width and highlights the faster wind-farm wake recovery in case A, which becomes evident about 4 km downstream of the wind-farm exit, at $x - x_0 \sim 12$ km. These variations in wind-farm wake recovery emphasize the crucial role of boundary-layer processes. Cloud-top cooling enables faster wake recovery, with both the inversion-layer height and turbulence intensity serving as key control factors. Consistent with this result, Lanzilao and Meyers [11] showed that even with identical turbulence intensity at hub height, a deeper boundary layer leads to faster wake recovery. Therefore, the deepening of the boundary layer caused by cloud-top cooling creates a

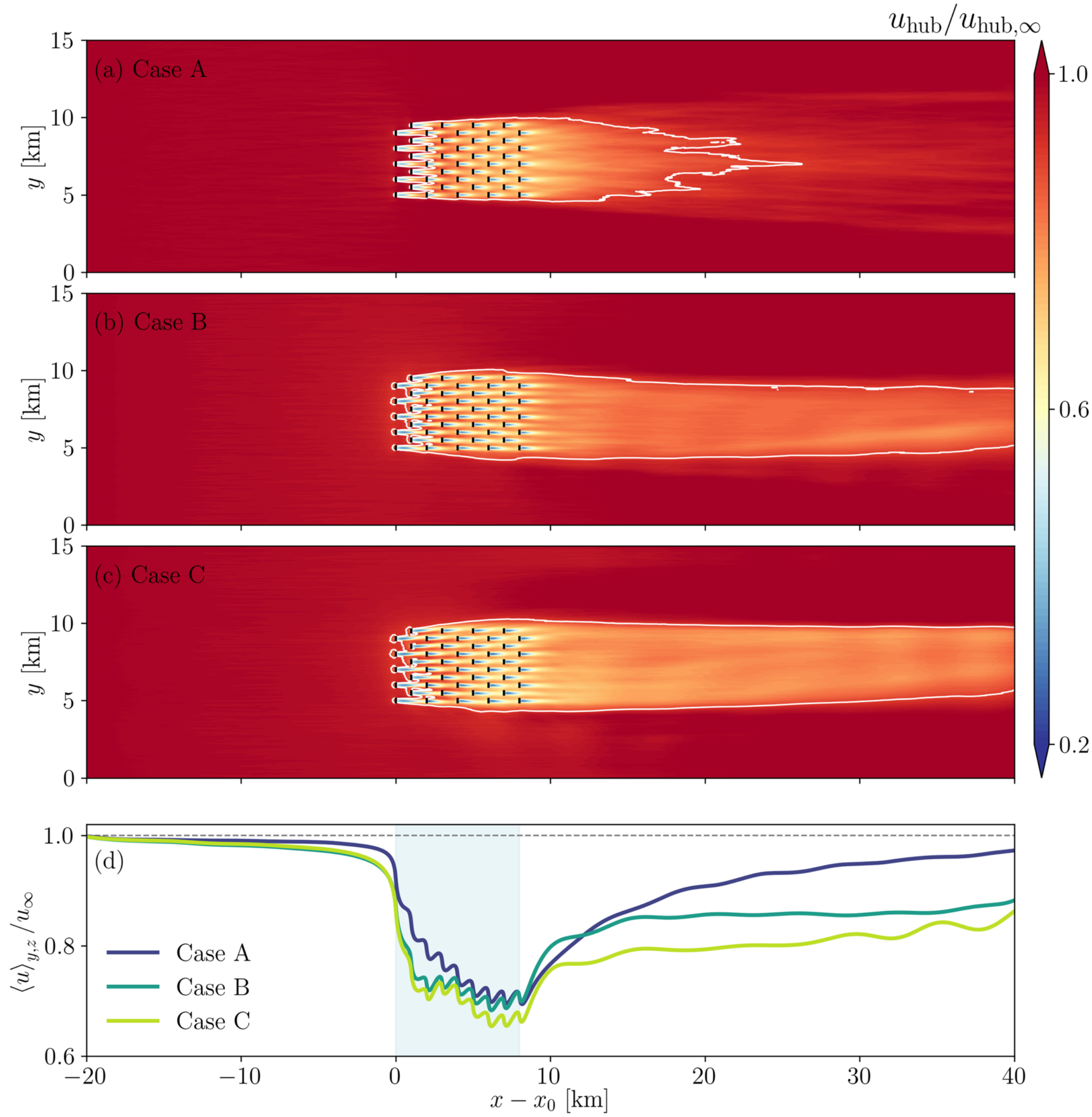

FIG. 6. (a), (b), (c) Time-averaged wind speed at hub height, normalized by the inflow velocity. Contours indicate regions where $u/u_{\mathrm{hub}} = 0.9$ for each case. (d) Comparison of the streamwise evolution of the velocity for the three cases, normalized by the respective inflow velocities and averaged across the wind-farm span and rotor height. The light-blue-shaded region marks the wind farm location.

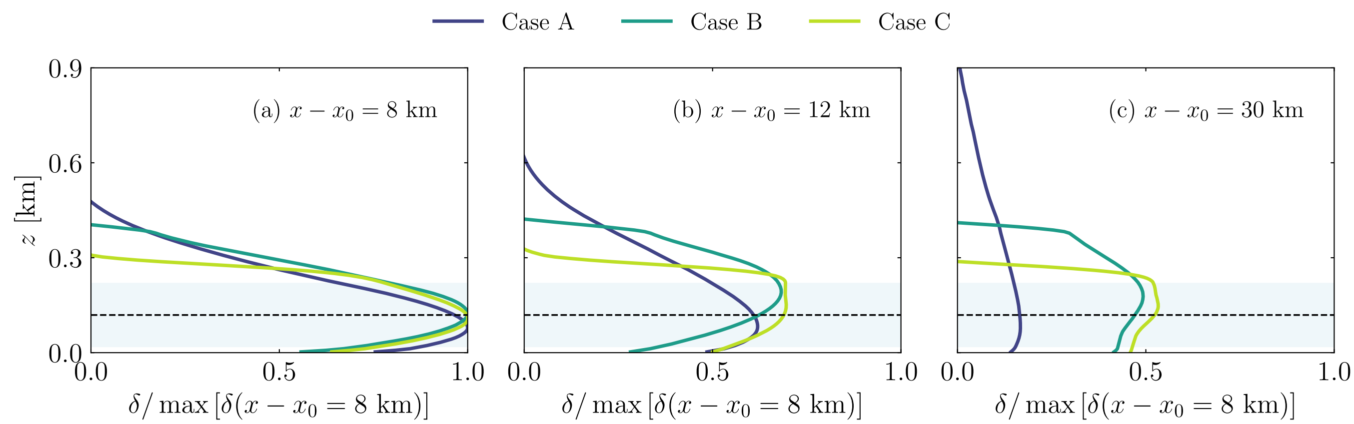

FIG. 7. Comparison of the normalized velocity deficit at three downstream locations of the wind farm: (a) $x - x_0 = 8$ km, (b) $x - x_0 = 12$ km, and (c) $x - x_0 = 30$ km. The light-blue shaded region denotes the rotor-swept area, and the dashed line indicates the hub height.

favorable environment for wake recovery, and the associated increase in turbulence intensity further facilitates this process.

To understand the different wake-recovery mechanisms among the cases, Fig. 7 presents the vertical velocity deficit δ, defined as the relative difference between the local velocity magnitude and the inflow velocity at hub height. To highlight the recovery immediately downstream of the wind farm, δ is normalized by its value at the wind-farm exit ($x - x_0 = 8$ km). Vertical profiles are displayed at three downstream locations: the wind-farm exit [panel (a), $x - x_0 = 8$ km], the near-wake region [panel (b), $x - x_0 = 12$ km], and the far-wake region [panel (c), $x - x_0 = 30$ km]. At the wind-farm exit, the wake structure is similar for all cases. However, noticeable differences in wake recovery already appear 4 km downstream [panel (b)]. Although the velocity deficit at hub height is comparable for cases A and B [see Fig. 6(d)], the wake in case A extends to higher altitudes above the wind farm ($z \gtrsim 0.3$ km). This increased vertical extent becomes even more evident in the far-wake region at $x - x_0 = 30$ km [Fig. 7], consistent with the faster downstream recovery seen in case A.

Multiple physical mechanisms contribute to the enhanced wind-farm wake recovery. In cases B and C, recovery immediately downstream of the wind farm (within the first 4 km) benefits from the presence of a supergeostrophic jet just above the farm, a characteristic feature of shallow boundary layers [10,54]. This jet is absent in case A (see Fig. 3), and previous works show that it is able to enhance energy entrainment into both the wind farm and its wake [11,51,52]. Farther downstream, other boundary-layer processes dominate wake recovery. In case A, the larger momentum flux and higher turbulence intensity enable stronger energy entrainment into the wake through larger-scale motions. In contrast, the lower inversion-layer height in cases B and C confines the wind-farm wake and the region to which it can draw additional momentum to $z \lesssim 0.4$ km. To assess the relative importance of these mechanisms and determine the one that dominates wind-farm wake recovery, we analyze the mechanical energy flux budget in Sec. IX.

VIII. WIND-FARM PERFORMANCE

Here we examine the wind-farm power production to assess whether differences in farm-wake recovery are related to turbine performance and wind turbine forcing. Figure 8 shows the row-averaged power production of each turbine row for the three cases. Panel (a) presents the absolute power, while panel (b) shows the power normalized by the first-row value. In this case, the first-row power produced in case A is higher than in the other cases, with a difference of approximately 5% compared with case C and 7% compared with case B. This is due to the higher boundary-layer height of case A, which decreases the blockage with respect to the other cases [Fig. 6(d)], due to which the velocity at the wind farm entrance is higher. Within the wind farm, the differences become more pronounced, particularly over the first three rows. This reflects the combined influence of boundary-layer entrainment and turbine-wake interactions on power production. In addition, turbine-induced gravity waves result in velocity oscillations that affect the power output of the downstream rows and reduce the overall wind farm efficiency [64]. This effect is more pronounced in cases B and C due to their lower inversion-layer heights. Farther downstream, beyond row 5, the power production becomes similar across all cases. Here, the maximum differences between the three simulations are about 5% in rows 8 and 9, as shown in both panels.

Although the presence of clouds can also influence the power output of wind farms, the relative similarity among the cases considered here, especially toward the end of the wind farm, likely results from two compensating effects:

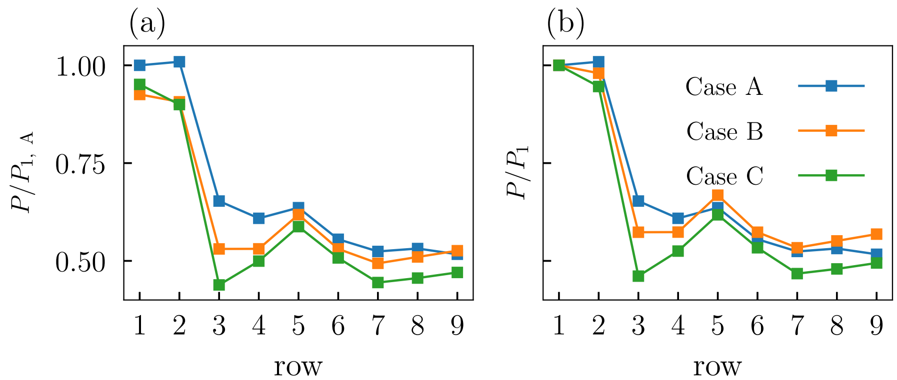

FIG. 8. Comparison of the row-averaged wind-farm power production as a function of turbine row. (a) Turbine power normalized by the maximum first-row value across all cases. (b) Turbine power normalized by the first-row value of each case.

the higher inflow velocities in cases B and C (Fig. 3) but lower boundary-layer height, which tend to increase blockage intensity; and the lower inflow velocity but higher inflow turbulence intensity and boundary-layer height in case A. However, the similarity in the power output is advantageous in this case, as it allows the wake-recovery mechanisms to be examined independently of large differences in turbines forcing the flow. In general, inversion-layer height, turbulence intensity, and inversion strength can lead to substantial variations in power production (see, e.g., Lanzilao and Meyers [10]); therefore, the present results should not be interpreted as representative of the overall cloud impact on wind-farm power. Instead, they confirm that the observed differences in far-wake recovery are primarily controlled by boundary-layer structure rather than by variations in turbine thrust.

IX. ENERGY FLUXES GOVERNING WIND-FARM WAKE RECOVERY

To study the processes governing near- and far-wake recovery, in this section, we analyze the energy contributions that drive wake recovery, providing insights relevant for future modeling efforts [63,67,68]. To this end, we consider the kinetic energy flux budget, obtained by multiplying the momentum (Eq. 2) by u_i:

$$\frac{1}{2}\frac{\partial u_i^2}{\partial t}+\frac{1}{2}\frac{\partial u_i^2 u_j}{\partial x_j}=-\frac{1}{\rho_{\text{ref}}}u_i\frac{\partial p}{\partial x_i}-u_i\frac{\partial \tau_{ij}}{\partial x_j}+\delta_{i3}u_i g\beta + \epsilon_{ij3}f_c u_i(u_j-u_G). \tag{9}$$

In this formulation, the filtering operator $\tilde{\cdot}$ is omitted for simplicity, and the turbine forcing is not included because it vanishes in the wake. After time averaging, applying the continuity equation, and rearranging terms, one obtains the following x-dependent balance equation for the mechanical energy flux $\mathcal{M}$ [69]. Each term $\delta\square$ is averaged over the spanwise and vertical areas swept by the rotors.

$$\begin{aligned}\int_{L_w}\underbrace{\left\langle \partial_{x_j}\left(\overline{u_j}\left(\frac{1}{2}\overline{u_i}\,\overline{u_i}+\frac{1}{2}\overline{u_i'u_i'}\right)+\frac{1}{\rho_{\text{ref}}}\left(\overline{p}\,\overline{u_i}+\overline{p'u_j'}\right)\right)\right\rangle_{y,z}}_{\delta\mathcal{M},\ \text{Mechanical energy flux}}dx \\ =-\int_{L_w}\underbrace{\left\langle \partial_{x_j}\left(\frac{1}{2}\overline{u_j'u_i'u_i'}+\overline{u_i}\,\overline{u_i'u_j'}+\overline{u_i\tau_{ij}}\right)\right\rangle_{y,z}}_{\delta\mathcal{T}_t,\ \text{Turbulent transport}}dx \\ +\int_{L_w}\underbrace{\left\langle f_c\overline{u_i}u_G\delta_{i2}-f_c\overline{u_i}v_G\delta_{i1}\right\rangle}_{\delta\mathcal{G},\ \text{Geostrophic forcing}}dx \\ +\int_{L_w}\underbrace{\left(-\left\langle\overline{\tau_{ij}S_{ij}}\right\rangle_{y,z}\right)}_{\delta\mathcal{D},\ \text{Dissipation}}dx-\int_{L_w}\underbrace{\left\langle g\delta_{i3}\,\overline{u_i\beta}\right\rangle_{y,z}}_{\delta\mathcal{B},\ \text{Buoyancy}}dx.\end{aligned} \tag{10}$$

where S_{ij} is the rate of strain tensor, $S_{ij}=1/2(\partial u_i/\partial x_j+\partial u_j/\partial x_i)$. When integrated along the wake extension L_w, Eq. (10) becomes

$$\mathcal{M}=-\mathcal{T}_t+\mathcal{G}+\mathcal{D}-\mathcal{B}. \tag{11}$$

On the left-hand side, $\mathcal{M}$ includes the contributions from kinetic energy and pressure work and represents the flux of mechanical energy that promotes wake recovery. The terms on the right-hand side act as sources or sinks of mechanical energy flux, thereby either enhancing or impeding wake recovery. Specifically, $\mathcal{T}_t$ denotes turbulent energy transport, including subgrid-scale (SGS) fluxes; $\mathcal{G}$ represents the contribution from large-scale geostrophic forcing; $\mathcal{D}$ corresponds to energy dissipation; and $\mathcal{B}$ accounts for energy production or dissipation due to buoyancy effects. To isolate the impact of the wind farm, the budget is evaluated relative to the inflow domain.

The top panels of Fig. 9 show the streamwise evolution of the energy-balance equation in the wind-farm wake. This allows us to assess the roles of energy production, dissipation, and transport in wake recovery. In all cases,

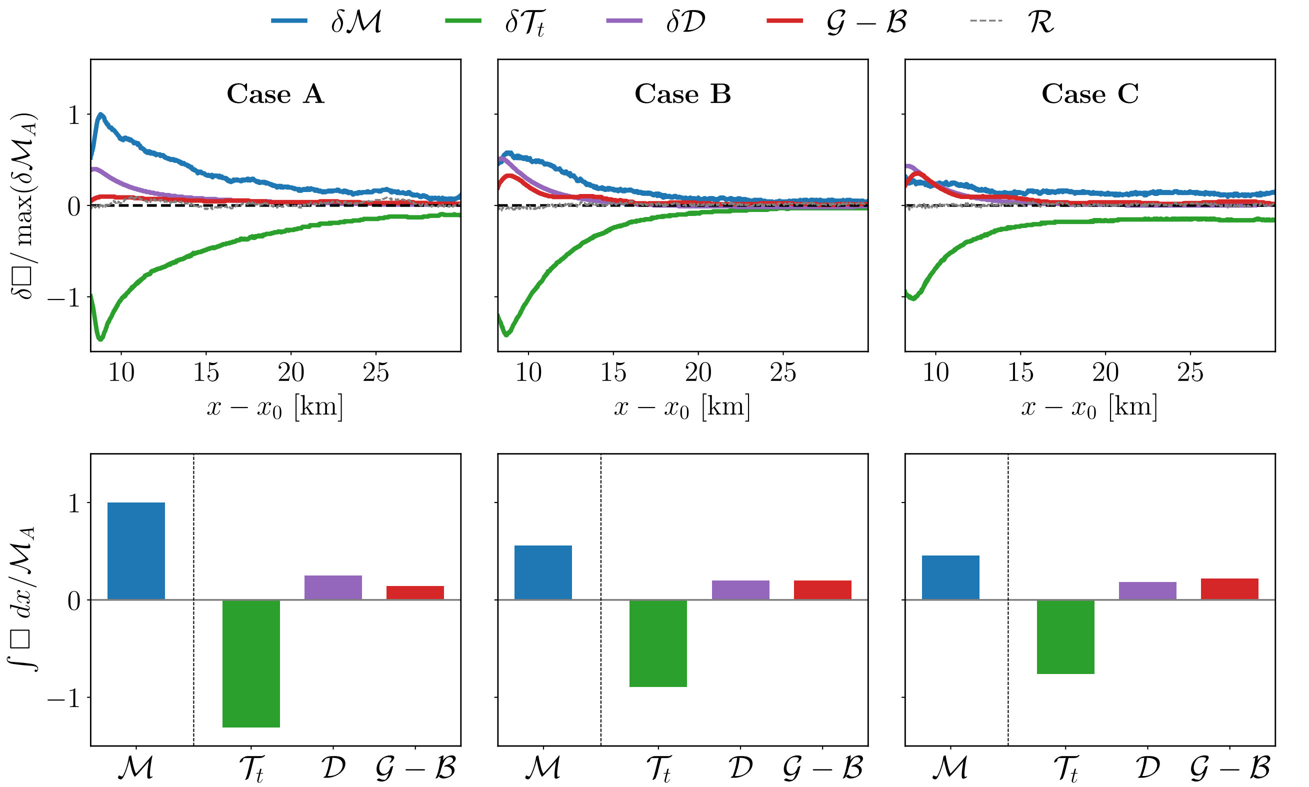

FIG. 9. Comparison of the energy-budget components for cases A, B, and C. The top panels show the streamwise evolution of the individual components, while the bottom panels show their cumulative integrals along the wake.

the residual, defined as the algebraic sum of all terms and accounting for numerical and time-convergence errors, remains close to zero. All budget terms decay with x before the streamwise velocity has recovered its upstream value in the wind-farm wake (Fig. 6). This reflects the faster adjustment of turbulence to the perturbation due to the wind farm. The contributions of $\mathcal{D}$ and $\mathcal{G}-\mathcal{B}$ are of lower magnitude and peak near the wind-farm exit due to the wind-farm-added k (see Fig. 5), before decaying downstream. In contrast, $\delta\mathcal{M}$ and $\delta\mathcal{T}_t$ retain larger magnitudes throughout the wake. This shows that turbulent energy transport is the dominant contributor to wind-farm wake recovery. When the transport is further decomposed into horizontal and vertical components, the vertical contribution dominates (not shown). This indicates a downward transfer of energy from higher atmospheric layers to the wind-farm region [69].

To quantify the cumulative contribution of each term within the wake, the bottom panels of Fig. 9 show their integrals from one rotor diameters downstream of the wind-farm exit, that is, from $x - x_0 = 8.2$ km to $x - x_0 = 25$ km (see Fig. 4). In case A, the mechanical energy flux $\mathcal{M}$ is larger than in the other cases, indicating a higher energetic content in the wake and promoting faster recovery. This behavior is consistent with the elevated k in the stratocumulus-topped boundary layer with cloud-top cooling (see Fig. 3). Further insight is provided by the ratio $-\mathcal{T}_t/\mathcal{M}$, which quantifies the relative contribution of turbulent transport to the mechanical energy flux. Case C shows the largest magnitude of this ratio, indicating that downward turbulent energy transport is more effective relative to the available mechanical energy than in case A. At the same time, case A features the largest available momentum flux, which favors the strongest overall entrainment into the wake.

In the cases considered, wake recovery is mainly governed by turbulent energy transport. To examine its spatial structure in the (x, z) plane, we analyze the vertical component of the turbulent transport flux $\langle\bar{u}\,\overline{u'w'}\rangle$. Figure 10 shows the evolution of this flux in and downstream of the wind farm, where its contribution to $\mathcal{T}_t$ is largest. The results show a clear downward transport of k from the upper to the lower parts of the boundary layer. Both the magnitude and the vertical extent of $\langle\bar{u}\,\overline{u'w'}\rangle/u_{\mathrm{hub}}^3$ depend strongly on the boundary-layer properties. In case A, consistent with the k field shown in Fig. 5, the region of downward energy transport extends farther downstream and up to heights of about 1 km. This behavior results from enhanced mixing in the stratocumulus-topped boundary layer due to cloud-top cooling and increased turbulence near the cloud top. In case B, the flux reaches a similar magnitude within the wind farm but is more vertically confined, while in case C, it is further reduced. In both cases B and C, the flux remains below $z \sim 0.4$ km, limited by the inversion-layer height. As a result, both

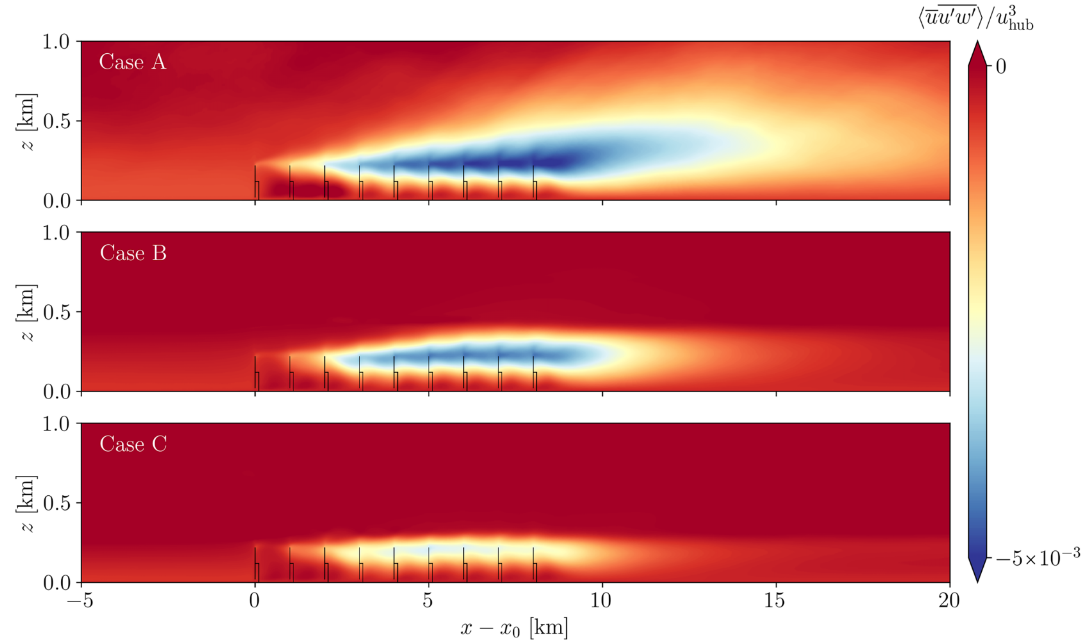

FIG. 10. Vertical energy flux for the three cases, averaged across the wind-farm span and normalized by the inflow velocity magnitude at hub height for each case.

the downward transport of energy and the energy available for wake recovery are reduced compared to case A.

Previous works demonstrate that the energy entrainment into the wind farm is favored by intense supergeostrophic jets above the turbine layer [51,52]. For this reason, the magnitude of $\langle \bar{u}\, \overline{u'w'} \rangle$ is larger in case B than in case C (see Fig. 10), reflecting the combined influence of the strength of the supergeostrophic jet and of the inversion-layer height. In case B, the region of downward energy transport extends to approximately $x - x_0 \sim 12$ km. Beyond this point, the jet weakens and wake recovery slows down, and wake recovery in case A becomes quicker than in case B (see Figs. 6 and 7). In conclusion, the presence of the supergeostrophic jet is favorable only in the near-wake of the wind farm, while farther downstream, the higher turbulence intensity and momentum flux availability of case A become dominant, thereby enhancing the wake recovery in the far-wake region.

X. CONCLUSIONS

We showed that the presence of low-level clouds in atmospheric boundary layers can be beneficial for the wake recovery of large offshore wind farms. To understand the underlying mechanisms, we examined three idealized scenarios using high-resolution Large Eddy Simulations: (A) a full stratocumulus-topped boundary layer (STBL), (B) a cloud-topped boundary layer without cloud-top radiative cooling, and (C) clear-sky conditions. These cases progressively remove specific physical processes, allowing us to clearly attribute differences in wake recovery to cloud-top radiative cooling and thus to the presence of the cloud. We find that the strong cloud-top radiative cooling introduced by low-level clouds promotes entrainment, deepens the boundary layer, and leads to enhanced turbulence intensity.

Analysis of wind-farm wakes using an energy-balance approach shows that far-wake recovery occurs much faster in the STBL than in other cases. In the near wake, recovery is initially faster in the shallower boundary layers due to low-level supergeostrophic jets, but this effect reduces downstream as the jet weakens. In the far wake, the deeper STBL facilitates a more effective replenishment of kinetic energy due to stronger atmospheric convection and a higher boundary-layer height. The energy-budget analysis connects this improved recovery to increased momentum flux and stronger turbulence, which enhance downward turbulent energy transport. Instead, the shallower inversion layers in the radiative cooling-free and clear-sky cases limit energy exchange between the free troposphere and the boundary layer, slowing wake recovery.

Overall, these results indicate that cloud-radiative effects can substantially influence wind farm-atmosphere interactions due to their impact on boundary-layer stability. This highlights an important process often overlooked in wind-farm wake models and power-loss calculations. Explicitly accounting for cloud-boundary layer coupling is therefore essential for improving wind-energy forecasts, especially in regions with frequent low-level cloud cover. A limitation of the current work is the lack of observational data supporting the effect on the wind-farm dynamics due to the presence of clouds and is motivated by the intrinsic difficulty in acquiring these data [24]. Therefore, future

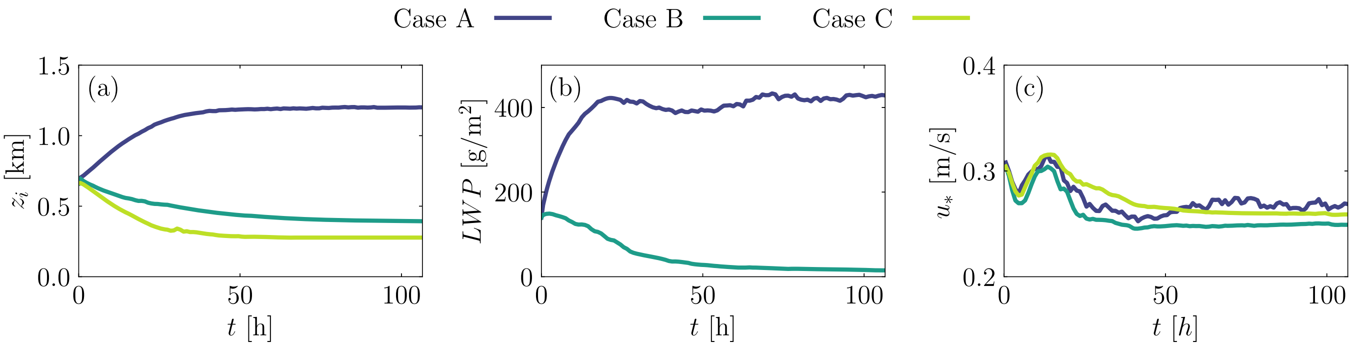

FIG. 11. Time evolution of the inflow boundary-layer properties. (a) Mean inversion-layer height. (b) Mean liquid water path [Eq. (8)]. (c) Mean surface friction velocity. Panel (b) excludes case C because its liquid water content is zero.

studies should expand on measurable effects of these interactions and should also include dynamically evolving and nonstationary conditions, such as transient clouds and mesoscale variability. Moreover, incorporating STBL dynamics into operational and reduced-order wind-farm models will be a key step toward more accurate power predictions and a deeper understanding of how wind farms impact the atmosphere. Beyond wind energy, these insights are also relevant to better understand the impact of wind farms on local atmospheric conditions.

ACKNOWLEDGMENTS

This project has received funding from the European Research Council (ERC) under the Horizon Europe program (Grant No. 101124815). We acknowledge the Gauss Centre for Supercomputing e.V. for project ID pr74sa on the GCS Supercomputer SuperMUC-NG at the Leibniz Supercomputing Centre. We acknowledge the Dutch national e-infrastructure of SURFsara, a subsidiary of SURF, the collaborative ICT organization for Dutch education and research. We acknowledge the project "2024.056" of the research programme "Computing Time on National Computing Facilities," co-funded by the Dutch Research Council (NWO).

DATA AVAILABILITY

The data are available from the authors upon reasonable request.

APPENDIX: STATISTICALLY STEADY-STATE CONDITIONS

To assess the statistical stationarity of the inflow conditions, we consider three key boundary-layer properties: the inversion-layer height z_i, the liquid water path LWP, and the surface friction velocity u_*. These quantities are integral measures of the boundary layer and are sensitive to boundary-layer forcings such as shortwave and longwave radiation, subsidence, and surface fluxes. When these quantities remain constant in time, the flow can be considered statistically stationary (see also van der Dussen *et al.* [43]). Figure 11 shows the time evolution of these boundary-layer properties. Panels (a) and (b) indicate that, in case A, boundary-layer growth is accompanied by an increase in LWP, whereas the opposite trend is observed in case B. This behavior results from enhanced entrainment of moisture and momentum from the free troposphere into the boundary layer due to cloud-top radiative cooling [14], which is absent in cases B and C. Case C shows a similar evolution to case B, reaching a lower inversion-layer height. Panel (c) shows the time evolution of the friction velocity. Its magnitude is similar in all cases and reaches a steady state after approximately 60 h, comparable to the equilibration time of z_i and LWP. This similarity arises from the use of identical surface boundary conditions and roughness height. Finally, after $t = 100$ h, all cases have reached statistically stationary conditions, and the results presented in this study are based on this time period [48].

[1] A. Platis, S. K. Siedersleben, J. Bange, A. Lampert, K. Bärfuss, R. Hankers, B. Canadillas, R. Foreman, J. Schulz-Stellenfleth, B. Djath, T. Neumann, and S. Emeis, *First in situ evidence of wakes in the far field behind offshore wind farms*, Sci. Rep. **8**, 2163 (2018).
[2] E. Finserås, I. H. Anchustegui, E. Cheynet, C. G. Gebhardt, and J. Reuder, *Gone with the wind? Wind farm-induced wakes and regulatory gaps*, Mar. Policy **159**, 105897 (2024).
[3] P. Veers *et al.*, *Grand challenges in the science of wind energy*, Science **366**, eaau2027 (2019).
[4] A. Kirby, T. Nishino, and T. D. Dunstan, *Two-scale interaction of wake and blockage effects in large wind farms*, J. Fluid Mech. **953**, A39 (2022).
[5] R. J. A. M. Stevens, *Understanding wind farm power densities*, J. Fluid Mech. **958**, F1 (2023).
[6] *Global wind power tracker, global energy monitor, february 2025* (2025), https://globalenergymonitor.org/projects/global-wind-power-tracker.
[7] C. J. Hahn and S. G. Warren, *A gridded climatology of clouds over land (1971-1996) and ocean (1954-2008) from surface*

observations worldwide, 10.3334/CDIAC/cli.ndp026e (ORNL Environmental Sciences Division, 2007).

[8] F. Porté-Agel, M. Bastankhah, and S. Shamsoddin, *Wind-turbine and wind-farm flows: A review*, Boundary Layer Meteorol. **174**, 1 (2020).

[9] R. J. A. M. Stevens and C. Meneveau, *Flow structure and turbulence in wind farms*, Annu. Rev. Fluid Mech. **49**, 311 (2017).

[10] L. Lanzilao and J. Meyers, *A parametric large-eddy simulation study of wind-farm blockage and gravity waves in conventionally neutral boundary layers*, J. Fluid Mech. **979**, A54 (2024).

[11] L. Lanzilao and J. Meyers, *Wind-farm wake recovery mechanisms in conventionally neutral boundary layers*, J. Fluid Mech. **1015**, A5 (2025).

[12] A. Stieren, J. H. Kasper, S. N. Gadde, and R. J. A. M. Stevens, *Impact of negative geostrophic wind shear on wind farm performance*, PRX Energy **1**, 023007 (2022).

[13] J. H. Kasper, A. Stieren, and R. J. A. M. Stevens, *Simulation and modeling of wind farms in baroclinic atmospheric boundary layers*, J. Renew. Sustain. Energy **16**, 6 (2024).

[14] R. Wood, *Stratocumulus clouds*, Mon. Weather Rev. **140**, 2373 (2012).

[15] V. P. Ghate, M. A. Miller, B. A. Albrecht, and C. W. Fairall, *Thermodynamic and radiative structure of stratocumulus-topped boundary layers*, J. Atmos. Sci. **72**, 430 (2015).

[16] J. P. Mellado, *Cloud-top entrainment in stratocumulus clouds*, Annu. Rev. Fluid Mech. **49**, 145 (2017).

[17] R. B. Stull, *An Introduction to Boundary Layer Meteorology* (Kluwer Academic Publishers, Dordrecht, The Netherlands, 1988).

[18] B. Stevens, *On the growth of layers of nonprecipitating cumulus convection*, J. Atmos. Sci. **64**, 2916 (2007).

[19] R. J. Hogan, A. L. M. Grant, A. J. Illingworth, G. N. Pearson, and E. J. O'Connor, *Vertical velocity variance and skewness in clear and cloud-topped boundary layers as revealed by Doppler lidar*, Q. J. R. Meteorol. Soc. **135**, 635 (2009).

[20] P. G. Duynkerke, S. R. de Roode, M. C. van Zanten, J. Calvo, J. Cuxart, S. Cheinet, A. Chlond, Hé Grenier, P. J. Jonker, M. Köhler, G. Lenderink, D. Lewellen, C-lyn Lappen, A. P. Lock, C-hoh Moeng, F. Müller, D. Olmeda, J-marcel Piriou, E. Sánchez, and I. Sednev, *Observations and numerical simulations of the diurnal cycle of the EUROCS stratocumulus case*, Q. J. R. Meteorol. Soc. **130**, 3269 (2004).

[21] D. Selvatici and R. J. A. M. Stevens, *"Gravity waves and blockage from offshore wind farms alter cloud albedo and surface fluxes"* (to be published).

[22] N. Akhtar, B. Geyer, and C. Schrum, *Impacts of accelerating deployment of offshore windfarms on near-surface climate*, Sci. Rep. **12**, 18307 (2022).

[23] N. Al Fahel and C. L. Archer, *Observed onshore precipitation changes after the installation of offshore wind farms*, Bull. Atmos. Sci. Technol. **1**, 179 (2020).

[24] A. Lampert *et al.*, *Airborne measurements for investigating offshore wind farm wakes and modifications of sea state: Benefits and limitations*, Wind Energy Sci. Discuss. **2026**, 1 (2026).

[25] B. Stevens, C.-H. Moeng, A. S. Ackerman, C. S. Bretherton, A. Chlond, S. de Roode, J. Edwards, J.-C. Golaz, H. Jiang, M. Khairoutdinov, M. P. Kirkpatrick, D. C. Lewellen, A. Lock, F. Müller, D. E. Stevens, E. Whelan, and P. Zhu, *Evaluation of large-eddy simulations via observations of nocturnal marine stratocumulus*, Mon. Weather Rev. **133**, 1443 (2005).

[26] J. P. Mellado, C. S. Bretherton, B. Stevens, and M. C. Wyant, *DNS and LES for simulating stratocumulus: Better together*, J. Adv. Model. Earth Syst. **10**, 1421 (2018).

[27] J. J. van der Dussen, S. R. de Roode, A. S. Ackerman, P. N. Blossey, C. S. Bretherton, M. J. Kurowski, A. P. Lock, R. A. J. Neggers, I. Sandu, and A. P. Siebesma, *The* GASS/EUCLIPSE *model intercomparison of the stratocumulus transition as observed during ASTEX: LES results*, J. Adv. Model. Earth Syst. **5**, 483 (2013).

[28] R. J. A. M. Stevens, M. Wilczek, and C. Meneveau, *Large-eddy simulation study of the logarithmic law for second- and higher-order moments in turbulent wall-bounded flow*, J. Fluid Mech. **757**, 888 (2014).

[29] S. N. Gadde, A. Stieren, and R. J. A. M. Stevens, *Large-eddy simulations of stratified atmospheric boundary layers: Comparison of different subgrid models*, Boundary- Layer Meteorol. **178**, 363 (2021).

[30] L. Liu, S. N. Gadde, and R. J. A. M. Stevens, *Universal wind profile for conventionally neutral atmospheric boundary layers*, Phys. Rev. Lett. **126**, 104502 (2021).

[31] C. Canuto, Y. M. Hussaini, A. Quarteroni, and T. A. Zang, *Spectral Methods in Fluid Dynamics* (Springer, Berlin, Heidelberg, 2012).

[32] C.-H. Moeng, *A large-eddy-simulation model for the study of planetary boundary-layer turbulence*, J. Atmos. Sci. **41**, 2052 (1984).

[33] J. D. Albertson and M. B. Parlange, *Surface length scales and shear stress: Implications for land-atmosphere interaction over complex terrain*, Water Resour. Res. **35**, 2121 (1999).

[34] F. Porté-Agel, C. Meneveau, and M. B. Parlange, *A scale-dependent dynamic model for large-eddy simulation: Application to a neutral atmospheric boundary layer*, J. Fluid Mech. **415**, 261 (2000).

[35] W. Rozema, H. J. Bae, P. Moin, and R. Verstappen, *Minimum-dissipation models for large-eddy simulation*, Phys. Fluids **27**, 085107 (2015).

[36] R. Verstappen, *When does eddy viscosity damp subfilter scales sufficiently?*, J. Sci. Comput. **49**, 94 (2011).

[37] J. P. Mellado, B. Stevens, H. Schmidt, and N. Peters, *Two-fluid formulation of the cloud-top mixing layer for direct numerical simulation*, Theor. Comput. Fluid Dyn. **24**, 511 (2010).

[38] G. Matheou and Jão Teixeira, *Sensitivity to physical and numerical aspects of large-eddy simulation of stratocumulus*, Mon. Weather Rev. **147**, 2621 (2019).

[39] P. J. Flatau, R. L. Walko, and W. R. Cotton, *Polynomial fits to saturation vapor pressure*, J. Appl. Meteorol. Climatol. **31**, 1507 (1992).

[40] D. Chung, G. Matheou, and J. Teixeira, *Steady-state large-eddy simulations to study the stratocumulus to shallow cumulus cloud transition*, J. Atmos. Sci. **69**, 3264 (2012).

[41] C. S. Bretherton, S. K. Krueger, M. C. Wyant, P. Bechtold, E. Van Meijgaard, B. Stevens, and J. Teixeira, *A GCSS boundary layer cloud model intercomparison study of the first ASTEX Lagrangian experiment*, Boundary Layer Meteorol. **93**, 341 (1999).

[42] P. G. Duynkerke, P. J. Jonker, A. Chlond, M. C. Van Zanten, J. Cuxart, P. Clark, E. Sanchez, G. Martin, G. Lenderink, and J. Teixeira, *Intercomparison of three- and one-dimensional model simulations and aircraft observations of stratocumulus*, Boundary Layer Meteorol. **92**, 453 (1999).

[43] J. J. van der Dussen, S. R. de Roode, S. Dal Gesso, and A. P. Siebesma, *An LES model study of the influence of the free tropospheric thermodynamic conditions on the stratocumulus response to a climate perturbation*, J. Adv. Model. Earth Syst. **7**, 670 (2015).

[44] E. J. Mlawer, S. J. Taubman, P. D. Brown, M. J. Iacono, and S. A. Clough, *Radiative transfer for inhomogeneous atmospheres: RRTM, a validated correlated-k model for the longwave*, J. Geophys. Res. **102**, 16663 (1997).

[45] S. K. Mehta, M. V. Ratnam, S. V. Sunilkumar, D. N. Rao, and B. V. Krishna Murthy, *Diurnal variability of the atmospheric boundary layer height over a tropical station in the Indian monsoon region*, Atmos. Chem. Phys. **17**, 531 (2017).

[46] A. M. Koning, L. Nuijens, F. C. Bosveld, A. P. Siebesma, P. A. van Dorp, and H. J. J. Jonker, *Surface-layer wind shear and momentum transport from clear-sky to cloudy weather regimes over land*, J. Geophys. Res. Atmos. **126**, e2021JD035087 (2021).

[47] S. Dal Gesso, A. P. Siebesma, and S. R. de Roode, *Evaluation of low-cloud climate feedback through single-column model equilibrium states*, Q. J. R. Meteorol. Soc. **141**, 819 (2014).

[48] M. Sanchez Gomez, J. K. Lundquist, J. D. Mirocha, and R. S. Arthur, *Investigating the physical mechanisms that modify wind plant blockage in stable boundary layers*, Wind Energy Sci. **8**, 1049 (2023).

[49] L. Lanzilao and J. Meyers, *An improved fringe-region technique for the representation of gravity waves in large eddy simulation with application to wind farms*, Boundary Layer Meteorol. **186**, 567 (2022).

[50] P. Marquet and B. Stevens, *On moist potential temperatures and their ability to characterize differences in the properties of air parcels*, J. Atmos. Sci. **79**, 1089 (2022).

[51] S. N. Gadde and R. J. A. M. Stevens, *Interaction between low-level jets and wind farms in a stable atmospheric boundary layer*, Phys. Rev. Fluids **6**, 014603 (2021).

[52] S. N. Gadde and R. J. A. M. Stevens, *Effect of low-level jet height on wind farm performance*, J. Renew. Sustain. Energy **13**, 013305 (2021).

[53] A. K. Blackadar, *Boundary layer wind maxima and their significance for the growth of nocturnal inversions*, Bull. Am. Meteorol. Soc. **38**, 283 (1957).

[54] J. G. Pedersen, S.-E. Gryning, and M. Kelly, *On the structure and adjustment of inversion-capped neutral atmospheric boundary-layer flows: Large-eddy simulation study*, Boundary Layer Meteorol. **153**, 43 (2014).

[55] P. Bortolotti, H. C. Tarrés, K. Dykes, K. Merz, L. Sethuraman, D. Verelst, and F. Zahle, *IEA wind TCP task 37: Systems engineering in wind energy-WP2.1 reference wind turbines*, National Renewable Energy Laboratory (NREL), Technical Report, 2019.

[56] A. Sescu and C. Meneveau, *A control algorithm for statistically stationary large-eddy simulations of thermally stratified boundary layers*, Q. J. R. Meteorol. Soc. **140**, 2017 (2014).

[57] C. R. Shapiro, D. F. Gayme, and C. Meneveau, *Filtered actuator disks: Theory and application to wind turbine models in large eddy simulation*, Wind Energy **22**, 1414 (2019).

[58] Y.-T. Wu and F. Porté-Agel, *Large-eddy simulation of wind-turbine wakes: Evaluation of turbine parametrisations*, Boundary Layer Meteorol. **138**, 345 (2011).

[59] Y.-T. Wu and F. Porté-Agel, *Simulation of turbulent flow inside and above wind farms: Model validation and layout effects*, Boundary Layer Meteorol. **146**, 181 (2013).

[60] R. J. A. M. Stevens, L. A. Martínez-Tossas, and C. Meneveau, *Comparison of wind farm large eddy simulations using actuator disk and actuator line models with wind tunnel experiments*, Renew. Energy **116**, 470 (2018).

[61] R. J. A. M. Stevens, J. Graham, and C. Meneveau, *A concurrent precursor inflow method for large eddy simulations and applications to finite length wind farms*, Renew. Energy **68**, 46 (2014).

[62] M. A. Khan, S. J. Watson, D. J. N. Allaerts, and M. Churchfield, *Recommendations on setup in simulating atmospheric gravity waves under conventionally neutral boundary layer conditions*, J. Phys. Conf. Ser. **2767**, 092042 (2024).

[63] K. S. Klemmer and M. F. Howland, *Momentum deficit and wake-added turbulence kinetic energy budgets in the stratified atmospheric boundary layer*, Phys. Rev. Fluids **9**, 114607 (2024).

[64] D. Allaerts and J. Meyers, *Boundary-layer development and gravity waves in conventionally neutral wind farms*, J. Fluid Mech. **814**, 95 (2017).

[65] D. Allaerts and J. Meyers, *Gravity waves and wind-farm efficiency in neutral and stable conditions*, Boundary Layer Meteorol. **166**, 269 (2018).

[66] D. Allaerts and J. Meyers, *Sensitivity and feedback of wind-farm-induced gravity waves*, J. Fluid Mech. **862**, 990 (2019).

[67] M. Bastankhah, M. M. Mohammadi, C. Lees, G. P. N. Diaz, O. R. H. Buxton, and S. Ivanell, *A fast-running physics-based wake model for a semi-infinite wind farm*, J. Fluid Mech. **985**, A43 (2024).

[68] K. S. Klemmer and M. F. Howland, *Wake turbulence modeling in stratified atmospheric flows using a novel k-ℓ model*, J. Renew. Sustain. Energy **17**, 3 (2025).

[69] J. H. Kasper and R. J. A. M. Stevens, *From turbine-scale to wind farm-scale wake recovery: Understanding the transition*, J. Renew. Sustain. Energy **18**, 1 (2026).